The East Australian Current and Property Transport at 27°S from 2012 to 2013

BERNADETTE M. SLOYAN, KEN R. RIDGWAY, AND REBECCA COWLEY

Commonwealth Scientific and Industrial Research Organisation, Ocean and Atmosphere Flagship, Hobart, Tasmania, Australia

(Manuscript received 14 March 2015, in final form 21 December 2015)

ABSTRACT

The East Australian Current (EAC) is the complex and highly energetic poleward western boundary current of the South Pacific Ocean. A full-depth current meter and property (temperature and salinity) mooring array was deployed from the continental shelf to the abyssal waters off Brisbane Australia (27°S) for 18 months from April 2012 to August 2013. The EAC mooring array is an essential component of the Australian Integrated Marine Observing System (IMOS). During this period the EAC was coherent with an eddy kinetic to mean kinetic energy ratio of less than 1. The 18-month, mean, poleward-only mass transport above 2000 m is 22.1 ± 7.5 Sverdrups (Sv; 1 Sv ≡ 10^6 m^3 s^{-1}). The mean, poleward-only heat transport and flow-weighted temperature above 2000 m are −1.35 ± 0.42 PW and 15.33°C, respectively. A difference in the poleward-only and net poleward mass and heat transports above 2000 m of 6.3 Sv and 0.24 PW reflects the presence of an equatorward EAC retroflection at the eastern (offshore) end of the mooring array. A complex empirical orthogonal function (EOF) analysis of the along-slope velocity anomalies finds that the first two modes explain 72.1% of the velocity variance. Mode 1 is dominant at periods of approximately 60 days, and mode 2 is dominant at periods of 120 days. These dominant periods agree with previous studies in the Tasman Sea south of 27°S and suggest that variability of the EAC in the Tasman Sea may be linked to variability north of 27°S.

1. Introduction

The East Australian Current (EAC) is the complex and highly energetic poleward western boundary current system of the South Pacific Subtropical Gyre. It is the dominant mechanism for the redistribution of heat between the ocean and atmosphere in the Australian region by transporting heat from the tropical Pacific Ocean to the midlatitude ocean and atmosphere. Between 10° and 15°S the South Equatorial Current (SEC) meets the Australian continental margin and bifurcates into the equatorward-flowing low-latitude western boundary currents [LLWBCs, encompassing the North Queensland Current (NQC) and the Gulf of Papua Current (GPC)] and the poleward East Australian Current (Ganachaud et al. 2014). The EAC strengthens as it flows southward between 27° to 33°S from 25 to 37 Sverdrups (Sv; 1 Sv ≡ 10^6 m^3 s^{-1}; Ridgway and Dunn 2003). The EAC typically separates from the western boundary at 31°–35°S, forming the broad eastward-flowing Tasman Front and a residual poleward flow at the western boundary, the EAC extension (Ridgway and Dunn 2003; Cetina-Heredia et al. 2014). The Tasman Front extends across the Tasman Sea to the northernmost tip of New Zealand, forming the East Auckland Current and a sequence of semipermanent eddies along the east coast of the New Zealand islands (Tilburg et al. 2001). The EAC extension consists of a series of eddies that propagate southward along the Australian coast as far south as Tasmania.

South of 30°S, the EAC is associated with a very energetic mesoscale eddy region (Boland and Hamon 1970; Boland and Church 1981; Everett et al. 2012). Given the dominance of mesoscale eddies, it is arguable whether the EAC is a single current at synoptic time scales, as the baroclinic eddy mass transport is several times that of the mean flow. Much of the eddy field is located on the continental slope and adjacent deep basin off the east coast of Australia, with the highest eddy activity between 30° and 37°S (Everett et al. 2012). The EAC and its eddies frequently move onto the continental shelf and influence the local circulation patterns. EAC eddy interaction with prominent topographic

Corresponding author address: Bernadette M. Sloyan, CSIRO, Ocean and Atmosphere Flagship, GPO Box 1538, Hobart, TAS 7001, Australia.
E-mail: bernadette.sloyan@csiro.au

DOI: 10.1175/JPO-D-15-0052.1

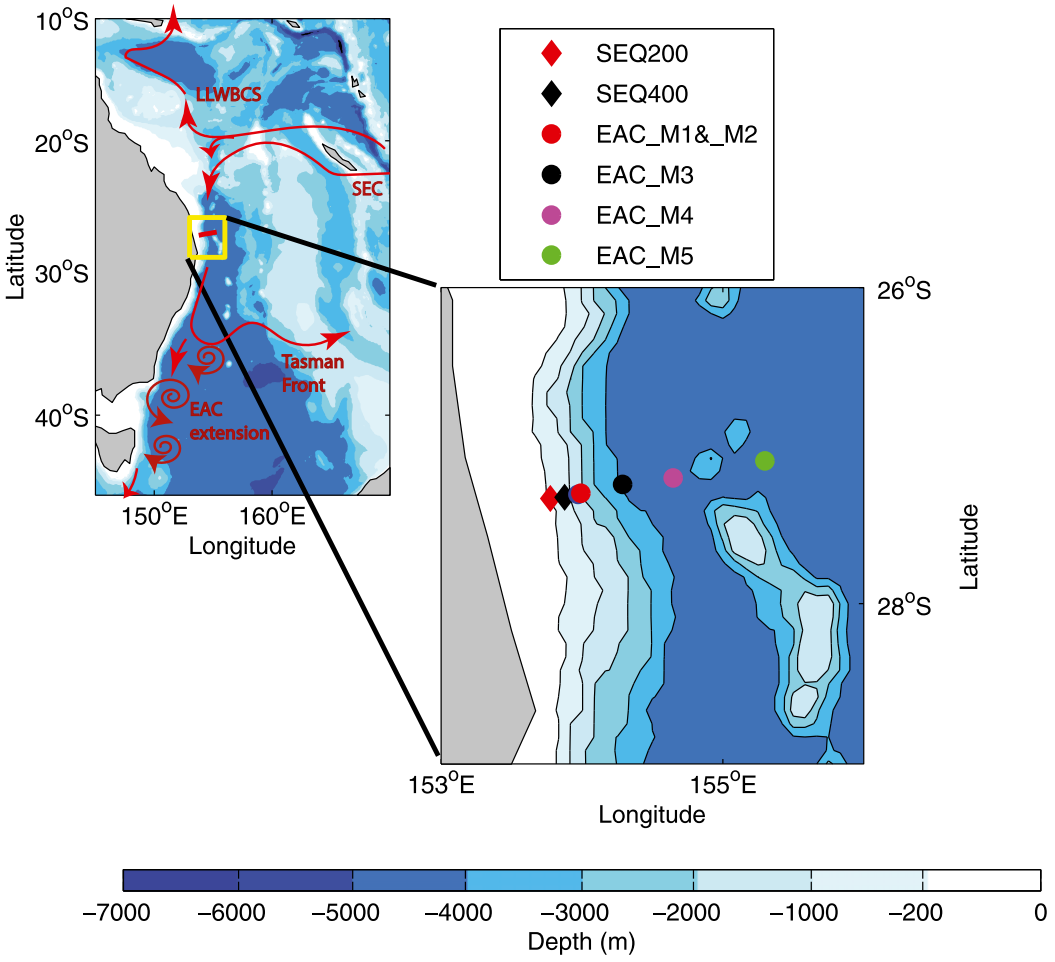

FIG. 1. Schematic of the major circulation features of the western Pacific and location of the mooring array. The major currents of the western Pacific shown are the SEC, LLWBCS, which include the NQC and GPC, EAC extension, and Tasman Front.

features (headlands and continental shelf) and wind-induced upwelling enhance the exchange of nutrient-rich subsurface water between the open ocean and coastal waters (Everett et al. 2014). Everett et al. (2014) suggest that changes in the strength of the EAC may have greater influence on shelf phytoplankton dynamics to the north of the separation zone.

The EAC shows variations over a range of time scales from seasonal to decadal. Much of our current understanding of the EAC has been developed from in situ observations collected over many decades. However, these data are irregularly distributed in both space and time and are not generally suitable for resolving changes in the EAC circulation over time periods ranging from interannual to decadal or longer time scales (Ridgway et al. 2002). After about 1990, surface observations of temperature and sea level collected from a diverse set of satellite platforms enable the seasonal, interannual, and decadal signals to be determined. Data from a long time series off the east coast of Tasmania (Maria Island Station) and the repeated, eddy-resolving XBT lines provide valuable in situ data (Ridgway 2007; Roemmich et al. 2005). However, none of these observations provide a comprehensive (spatial or temporal) description of the EAC.

Sustained monitoring of the EAC, and other western boundary currents, provides an essential ocean index that will result in an improved understanding of the variability of the strength and dynamics of these dominant boundary currents. The western boundary currents provide a link between the remote basin-scale forcing variability and the coastal boundary circulation (Sloyan and O'Kane 2015). Monitoring of the EAC will further improve our understanding of the impacts and influences of the large-scale remotely driven variability of the EAC and the response of the Australian east coast

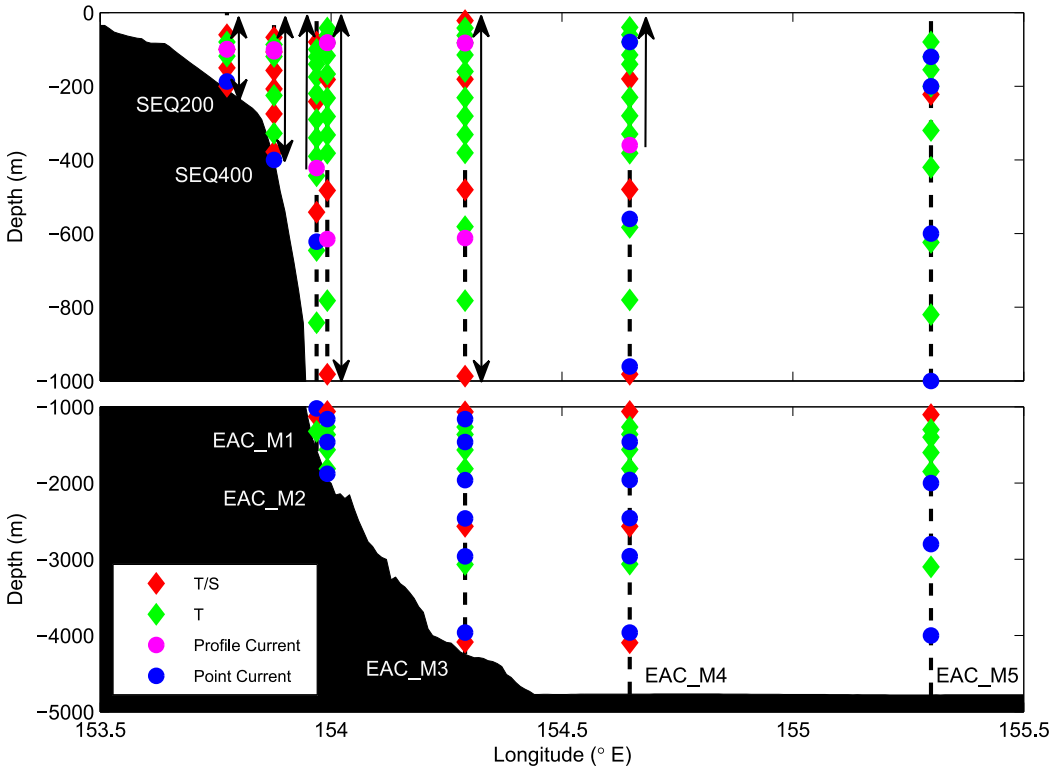

FIG. 2. Cross section of the mooring array on the continental slope and deep abyssal basin and instruments deployed on each mooring. The depth interval of velocity profiles provided by ADCP instruments (magenta circle) are shown by a black double-headed arrow (indicating upward- and downward-pointing ADCPs) or single-headed arrow (upward-looking ADCP). The depth of point-source velocity instruments (blue circles) are also shown. Depths of *T* instruments are shown as green diamonds, and *T*/*S* instruments are identified by red diamonds.

slope and shelf circulation systems. The links between basin-scale ocean and climate variability and the slope and shelf circulation is significant as this interaction impacts open ocean–coastal exchange (nutrient supply), mixing of coastal and shelf waters, and the variability of wind-driven coastal currents and upwelling (e.g., Everett et al. 2014). These dynamical processes impact the ecosystem structure and function (e.g., biodiversity) from monthly to multidecadal time scales.

While previous work, using the available observations and ocean models, has documented long-term trends and variability of the EAC and suggested a link between the EAC variability with the large-scale Pacific Gyre forcing (e.g., Ridgway et al. 2008; O'Kane et al. 2011; Cetina-Heredia et al. 2014; Oliver and Holbrook 2014; Sloyan and O'Kane 2015), an understanding of the full-depth EAC property transport and its temporal variability is far from complete. What is lacking from the observational network is a sustained time series of full-depth property observations of the boundary flow of the EAC across its entire offshore extent and of sufficient duration to resolve seasonal, interannual, and decadal signals. The only existing data are from a 2-yr mooring array at 30°S maintained during WOCE (Mata et al. 2000). However, this mooring array was only 120 km wide, and the complete extent of the EAC system was not resolved. This was compounded by the fact that the array was located within the most energetic portion of the EAC eddy field (Everett et al. 2012).

To fill this observational gap, the Australian Integrated Marine Observing System (IMOS) deployed a full-depth current meter and property [temperature (*T*) and salinity (*S*)] mooring array from the continental shelf to the abyssal waters across the EAC at approximately 27°S (Fig. 1). The initial EAC transport monitoring array was deployed from April 2012 to August 2013. The mooring array consisted of seven moorings ranging in water depth of 200 to 4797 m (Fig. 2).

This study provides the first estimates of the mean and variability of the EAC property transport at 27°S. It is envisaged that the EAC mooring array, which complements existing western boundary current monitoring efforts, will be an integral component of the Global

TABLE 1. Summary of mooring deployments.

Mooring name	Deployed (UTC)	Retrieved (UTC)	Location		Depth (m)
			Latitude (°S)	Longitude (°E)	
SEQ200	1 Apr 12	09 Jun 13	27.34	153.771	209
SEQ400	1 Apr 12	09 Jun 13	27.33	153.88	405
EAC_M1	1328 21 Apr 12	2130 23 Aug 13	27.31	153.97	1525
EAC_M2	0727 22 Apr 12	0430 24 Aug 13	27.31	153.997	1940
EAC_M3	1025 23 Apr 12	2229 24 Aug 13	27.25	154.297	4220
EAC_M4	0633 25 Apr 12	2320 25 Aug 13	27.21	154.65	4745
EAC_M5	0914 26 Apr 12	2224 26 Aug 13	27.10	155.30	4797

Ocean Observing System, providing the only sustained time series of EAC property transports.

2. Mooring array and data processing

The mooring array consisted of seven moorings in water depths of 200 to 4797 m and spanning a distance of 152.94 km from the continental shelf to the abyssal plain (Figs. 1, 2; Table 1). The moorings in 200 and 400 m of water were deployed as part of the IMOS coastal mooring program, and the remaining five continental slope and abyssal moorings were deployed by the deep-water program. Acoustic Doppler current profiling (ADCP) instruments of various frequencies (RDI ADCPs 75, 150, and 300 kHz) provide velocity profiles, at varying vertical resolution from 4 to 16 m, in the upper 1000 m. The ADCPs were deployed in various configurations including collocated upward and downward looking, downward looking, and upward looking. Point-source velocity data were obtained from Nortek Aquadopp instruments at varying vertical resolution of 500 to 1000 m.

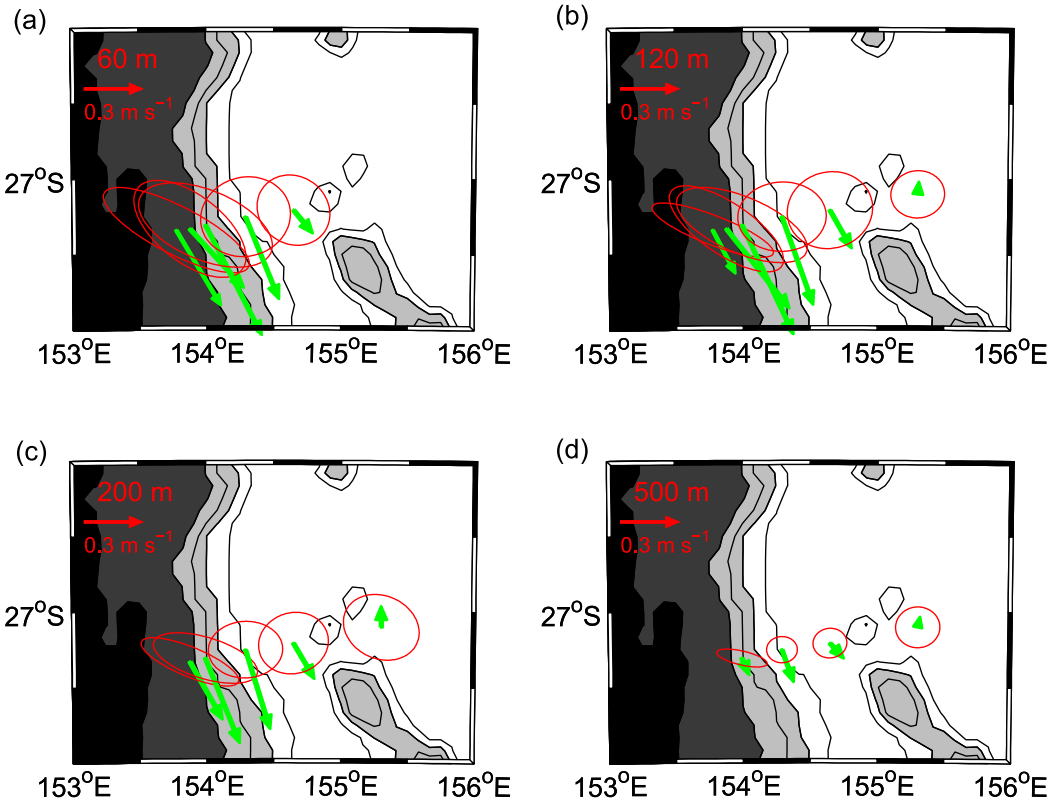

FIG. 3. Mean velocity (m s^{-1}, green arrow) and velocity variance ellipse (red circle) for (a) 60, (b) 120, (c) 200, and (d) 500 m. The 1000-, 2000-, 3000-, and 4000-m isobaths are contoured and topography shallower than 3000 m is shaded.

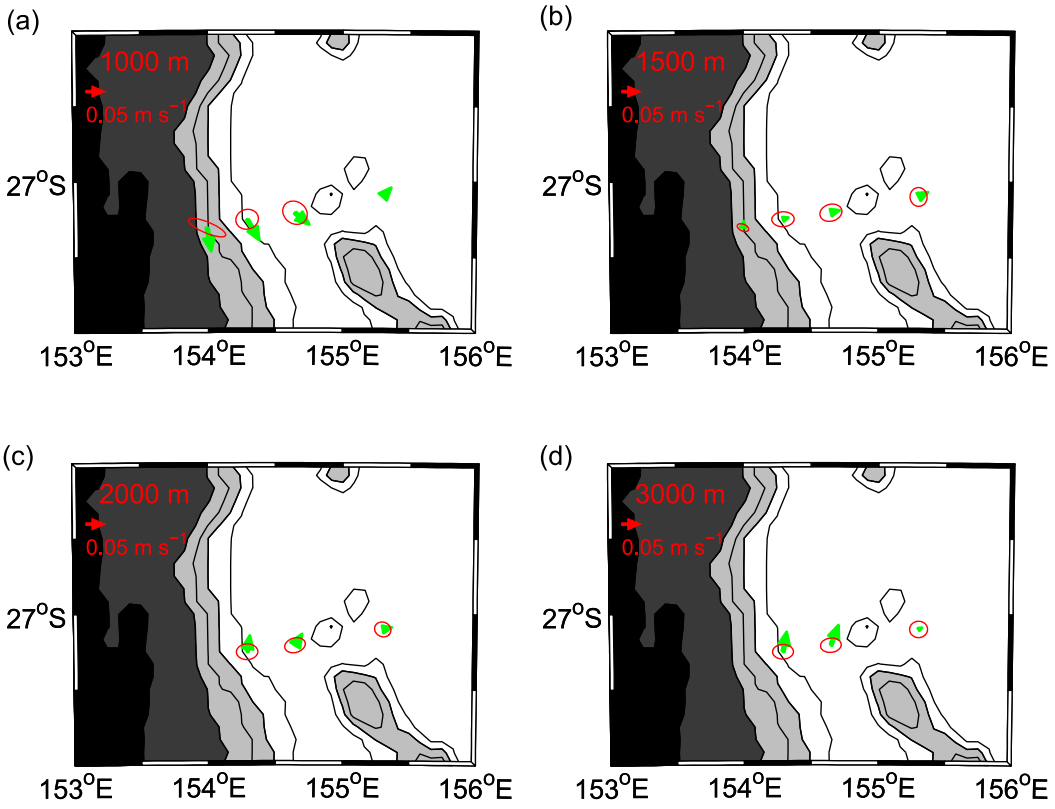

FIG. 4. Mean velocity vectors (m s^{-1}, green arrow) and velocity variance ellipse (red circle) for (a) 1000, (b) 1500, (c) 2000, and (d) 3000 m. The 1000-, 2000-, 3000-, and 4000-m isobaths are contoured and topography shallower than 3000 m is shaded.

On the SEQ200, SEQ400, EAC_M1, EAC_M2, and EAC_M3 moorings, ADCPs provide velocity observations from the sea surface to 1000 m (Fig. 2). Below 1000 m, velocity data are provided by Nortek Aquadopp instruments at 500-m vertical resolution to 2000 m and then 1000-m vertical resolution to the seafloor. The offshore EAC_M4 and EAC_M5 moorings were not as heavily instrumented for velocity as the inshore moorings (SEQ220, SEQ400, EAC_M1, EAC_M2, and EAC_M3). On EAC_M4 an ADCP (upward looking) at 360 m provides velocity observation at 16-m vertical resolution to the sea surface. Point-source velocity observations were obtained at varying vertical resolution (100 to 1000 m) from 80 m to the seafloor on EAC_M5.

Temperature observations were obtained from Sea-Bird Electronic (SBE) SBE39-plus, SBE37-SMP MicroCAT, and Starmon Mini instruments, and salinity observations came from Sea-Bird Electronic SBE 37-SMP MicroCAT (Fig. 2). All Sea-Bird instruments provide pressure observations. Prior to deployment, all Sea-Bird Electronic instruments were either calibrated at the CSIRO Marine and Atmospheric Research Calibration Facility or in the case of new instruments by the manufacturer. Calibration was not performed on the other instrument types prior to deployment. On retrieval of the moorings all temperature sensors were placed in a calibration bath. A calibrated Sea-Bird SBE37 was used to compare the instruments retrieved from the mooring. The

TABLE 2. Integral timescale (days) of across- and along-slope velocity records grouped by depth interval.

	Mooring											
	SEQ200		SEQ400		EAC_M2		EAC_M3		EAC_M4		EAC_M5	
Depth (m)	Across	Along	Across	Along	Across	Along	Across	Along	Across	Along	Across	Along
0–1000	3.8	3.9	6.0	6.4	4.4	11.5	4.0	7.3	6.2	6.9	8.8	20.9
1000–2000					4.3	5.5	9.7	13.9	10.5	8.3	8.3	20.3
2000–5000							15.6	14.1	8.7	10.4	10.0	16.1

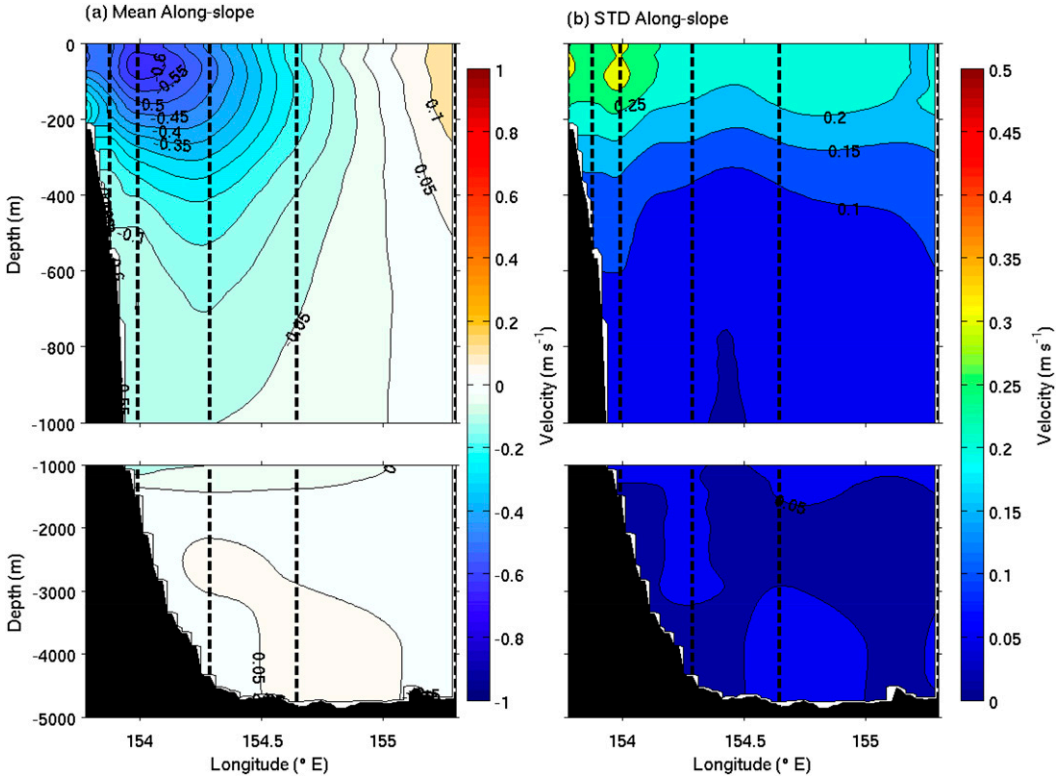

FIG. 5. The 18-month EAC along-slope (a) mean velocity (m s^{-1}) and (b) standard deviation (m s^{-1}). Contour intervals are 0.05 m s^{-1}. Also shown are the positions of the moorings (dashed lines).

calibration bath is not designed to give an accurate temperature offset for each instrument but rather indicate any large offset problems due to the long period on the mooring and fouling. A complete postdeployment calibration was performed on Sea-Bird instruments. Temperature data are resolved at 20-m vertical resolution from approximately 20 to 200 m, at 50-m vertical resolution from 200 to 400 m, at 100-m vertical resolution from 400 to 800 m, and at 200- to 300-m vertical resolution from 800 m to the seafloor. Salinity observations are resolved at a vertical resolution of 200 to 1000 m. Temperature and salinity vertical resolution is similar for all moorings.

A total of 143 instruments were deployed on the mooring array (Fig. 2). The velocity data return of instruments deployed was 87%. All mooring data are freely available from the IMOS data portal (https://imos.aodn.org.au/imos123/) and OceanSITES (http://www.oceansites.org). Here, we provide a brief summary of the data quality control and procedures applied. The reader is referred to Cowley (2015; http://data.aodn.org.au/IMOS/public/ABOS/reports/) for further information on mooring design and quality control procedures. We use the quality controlled time series to produce the gridded velocity and temperature data used in this study.

Processing and quality control of the data were completed using MATLAB routines (Cowley 2015) and the IMOS toolbox (https://github.com/aodn/imos-toolbox). A summary of the processing steps applied are as follows:

- Download data from instruments and collect metadata.
- Insert quality control (QC) flags using the IMOS standard QC set at the start and end of instrument deployment.
- Check for obvious timing errors.
- Check for large temperature offsets using the bath calibration data.
- Use the IMOS automated routine to flag spikes. Visually check the data quality of each parameter from each instrument in the context of data from adjacent instruments. Apply appropriate QC flags and apply offsets and adjust for drift if necessary and possible.
- Apply the local magnetic deviation to the ADCP compass and quality control the data.
- Stack the mooring data and infer depths for instruments without pressure sensors. Put the instrument data onto a common time base and apply further checks for temperature and pressure drifts and differences in current angles between adjacent current instruments.

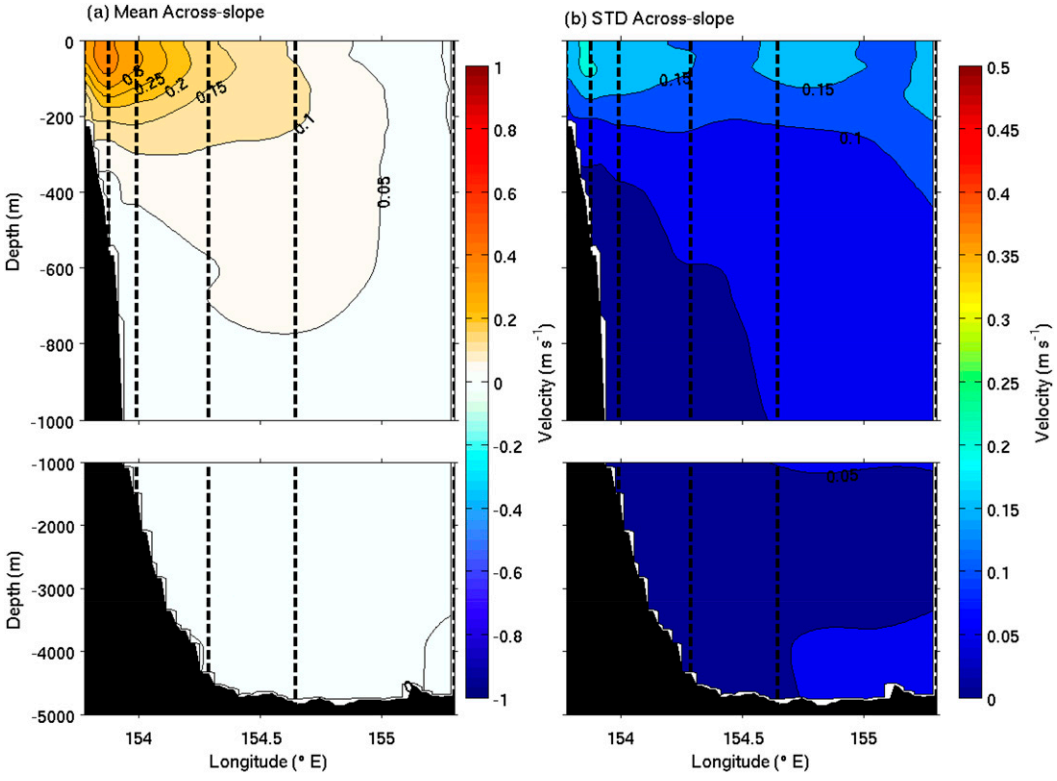

FIG. 6. As in Fig. 5, but for across-slope velocity.

The quality-controlled mooring data were then interpolated to a 10-m vertical grid between the sea surface and 400 m and to a 20-m vertical grid from 420 m to the seafloor. A 5-day filter was applied to the mooring data to remove tides, and all data were then interpolated to a common daily time series and a 2-km horizontal grid. Data were extended from the last good data point to the bottom of the continental slope iteratively using the mean of adjacent good data points. The velocity data are rotated −20° from true north to orientate the velocity with the primary axis of the continental slope (Fig. 1). We use this rotated velocity data in this analysis. Given that moorings EAC_1 and EAC_2 were only 2.4 km apart and that the data from the two moorings are highly correlated, we exclude data from EAC_1 in this analysis.

3. The EAC velocity and property transports

a. Velocity

The mean velocity vectors, calculated from the full 18-month time series, show poleward velocity from the sea surface to 1500 m across the continental shelf to EAC_M4 (154.65°E) and weaker equatorward velocity at EAC_M5 (155.30°E; Fig. 3). These results show that the mooring array captures the complete horizontal extent of the EAC current, being able to define the boundary between poleward flow of the EAC and the offshore equatorward recirculation. The variance ellipses show that the variability of the EAC is dominated by east–west variability of the velocity vector. Below 2000 m, the mean velocity vectors show a bottom intensification of equatorward flow at EAC_M3 and EAC_M4 (Fig. 4). The mean integral time scale of the mooring array, or decorrelation time scale, varies from 4 to 20 days (Table 2). In the upper 2000 m, the integral time scales of both the across- and along-slope velocity components are shortest at moorings on the continental shelf and inner slope (SEQ200, SEQ400, and EAC_M2) and increase in an eastward direction across the mooring array (Table 2). The integral time scale also increases with depth.

The 18-month mean along-slope velocity shows a poleward current extending from the continental shelf to approximately 155°E, a width of approximately 123 km, and from the sea surface to 1200 m (Fig. 5). There is a weaker equatorward velocity at the eastern edge of the mooring array (Fig. 5). The poleward EAC current core has a subsurface maximum velocity, centered at 60 m, of greater than 0.6 m s^{-1}. The subsurface velocity maximum is found slightly seaward of the continental slope. The EAC mooring array also reveals a

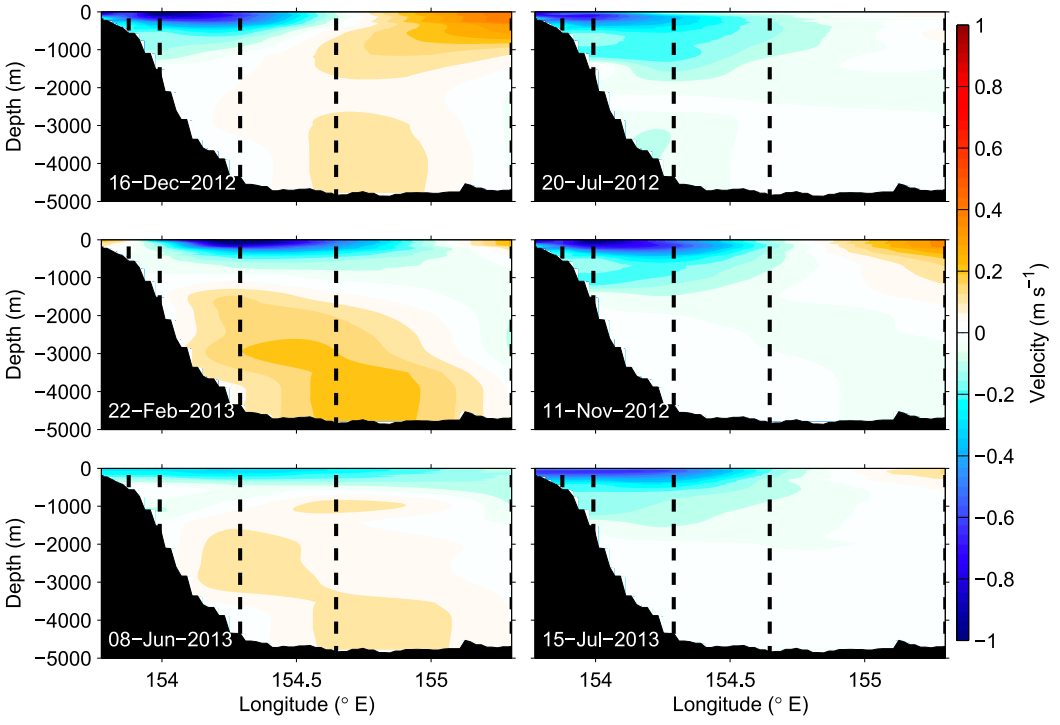

FIG. 7. Snapshots of the EAC along-slope velocity during the 18-month deployment period. Also shown are the locations of the moorings (black dashed lines). The mass transport at these times is shown in Fig. 10 as (left) dashed blue and (right) dashed magenta.

deep-ocean bottom-intensified equatorward velocity of greater than 0.05 m s^{-1}. The standard deviation of the along-slope current has three maxima: two associated with the EAC upper-ocean velocity and a maximum in the deep ocean. The largest standard deviation is found at the western edge of the mooring array with the maximum centered near the mean current core. The second relative maximum is found at the offshore eastern edge of the mooring array between 154.5° and 155.2°E. While the magnitude of the standard deviation at the EAC core is much smaller than the mean velocity, the standard deviation at the eastern edge of the EAC is of a comparable magnitude to the EAC mean velocity at this location. The deep-ocean standard deviation maximum is found below 3000 m, centered near 154.7°E. The mean across-slope velocity is only about a half of the along-slope velocity with a maximum eastward velocity of greater than 0.35 m s^{-1} on the continental shelf (Fig. 6). The across-slope velocity decreases to 0.25 m s^{-1} in the EAC poleward core. The across-slope velocity is surface intensified with velocities decreasing to less than 0.1 m s^{-1} below 250 m. The standard deviation of the across-slope velocity is of a similar magnitude to the mean. Not surprising, the along- and across-slope 18-month velocity mean shows that the poleward velocity of the EAC is the dominant feature across the mooring array.

The two maxima in the upper 300 m of the alongshore standard deviation (Fig. 5) suggest that the poleward EAC wavers back and forth in an onshore–offshore direction across the mooring array. Time series snapshots of the along-slope velocity distribution show the variation of the position of the EAC across the array (Fig. 7). On 16 December 2012 the poleward EAC extends to approximately 154.6°E and down the continental slope to 1500 m. A strong equatorward velocity—the EAC recirculation—is found to extend eastward of 154.7°E to the eastern edge of the mooring array (155.30°E). At other times (20 July 2012 and 8 June 2013), the EAC poleward velocity extends across the entire mooring array; however, the alongshore velocity core of the EAC is still contained within the mooring array (Fig. 7). On 11 November 2012 and 15 July 2013 the edge of equatorward velocity of the EAC recirculation is found at the outer edge of the mooring array. At 22 February 2013, the poleward core of the EAC has moved offshore to be centered at approximately 154.2°E, and there is an equatorward along-slope velocity over the continental shelf at the western edge of the mooring array (Fig. 7). This time slice also shows strong deep (below 3000 m) equatorward velocity of approximately 0.2 m s^{-1}. This strong deep velocity, although not the focus of the current

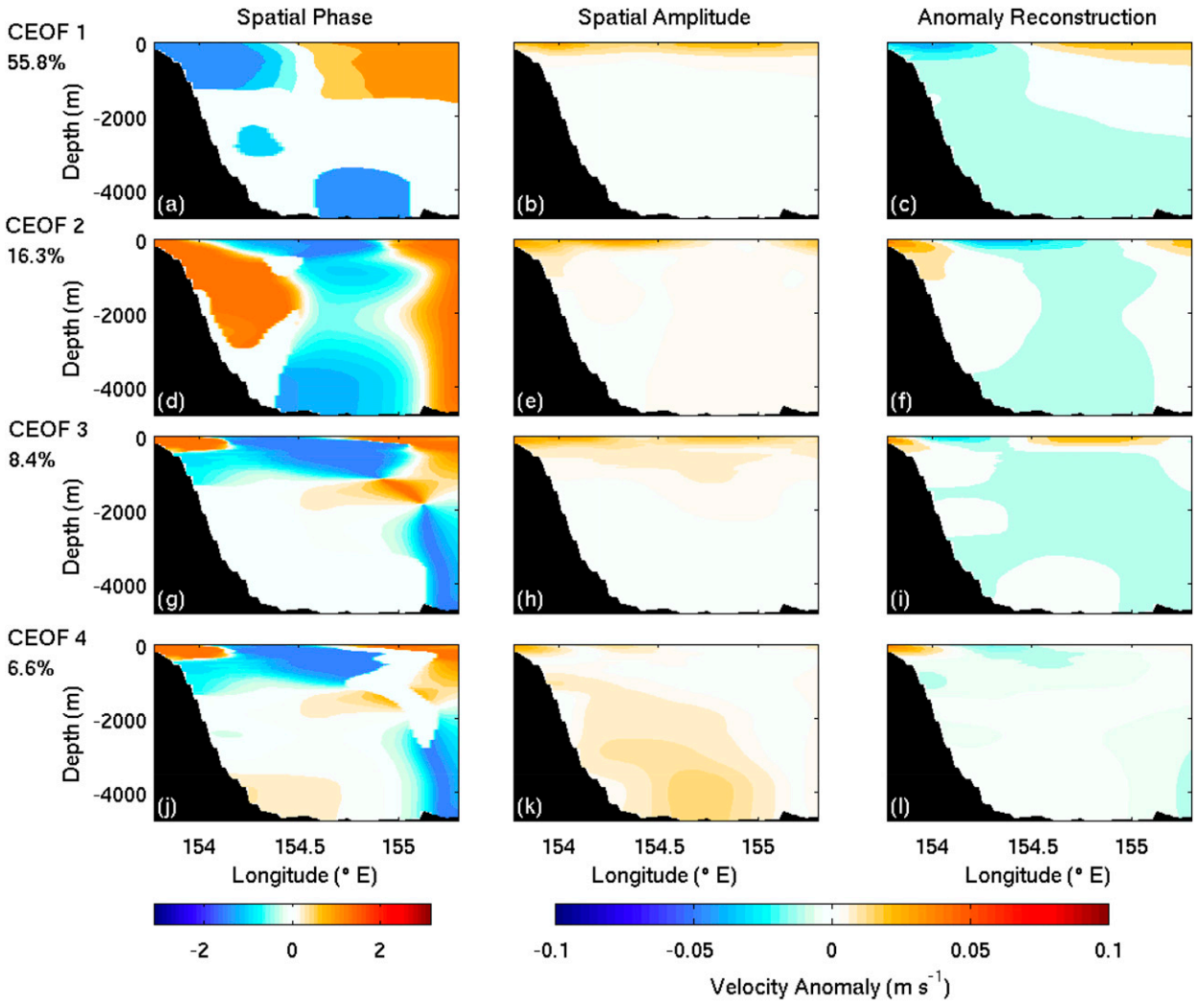

FIG. 8. The EAC velocity anomaly first four modes of the CEOF. For each mode the spatial maps of the (a),(d),(g),(j) phase ($-\pi$ to π) and (b),(e),(h),(k) amplitude and (c),(f),(i),(l) reconstructed velocity anomaly ($m\,s^{-1}$) are shown. The percentage of the anomaly explained by each mode is 55.8% for mode 1, 16.3% for mode 2, 8.4% for mode 3, and 6.6% for mode 4. The phase is only shown where the amplitude is > 0.02. The reconstructed velocity anomaly for each mode is determined from the spatial amplitude and phase maps.

work, highlights the fact that the abyssal ocean at 27°S is far from quiescent.

b. *Time series analysis using complex empirical orthogonal function*

The horizontal and vertical variations in the position of the EAC during the time series suggest that the EAC current propagates across the mooring array. While conventional empirical orthogonal functions (EOFs) are applied to stationary fields, complex empirical orthogonal functions (CEOFs) are more appropriate for nonstationary propagating time series (Hannachi et al. 2007). The along-slope velocity anomaly time series are Hilbert transformed to create a complex along-slope velocity anomaly time series. EOFs are computed using the singular value decomposition.

The CEOF analysis of the along-slope velocity anomalies show that the wavering of the EAC across the mooring array can be explained by the first four leading modes (Fig. 8). The phase and amplitude spatial maps of mode 1 has the EAC along-slope anomaly pattern extending from the continental shelf to approximately 154.3°E and to depths of 1200 m and the EAC retroflection extending eastward from 154.7°E to the eastern boundary of the mooring array (Figs. 8a,b). The mode-1 velocity anomaly reconstruction shows that this mode defines the situation when the poleward EAC is located on the continental shelf and extends eastward to approximately 154.5°E, and farther offshore the equatorward

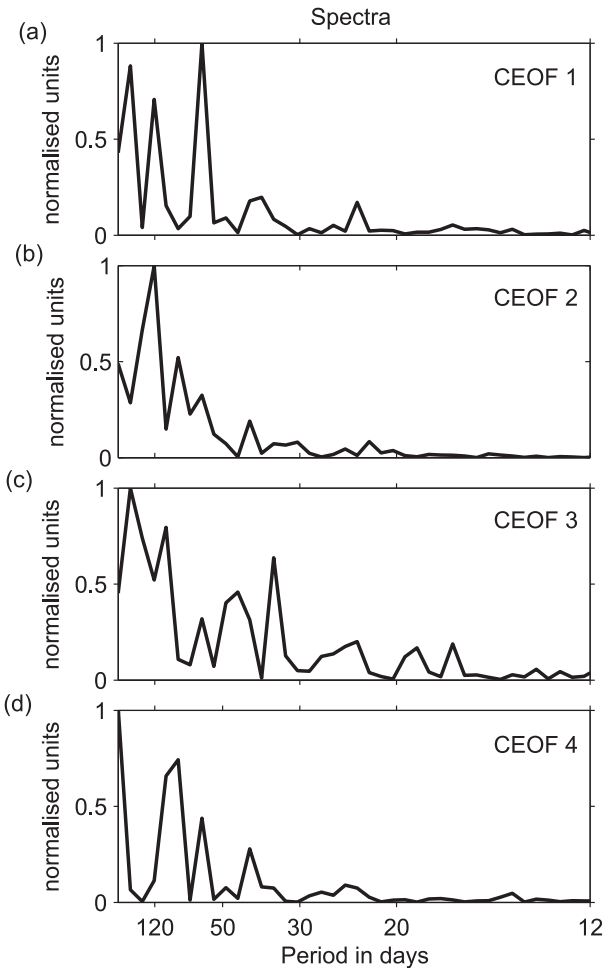

FIG. 9. The normalized EAC velocity anomaly spectra of (a) mode 1, (b) mode 2, (c) mode 3, and (d) mode 4. The percentage of the anomaly explained by each mode is shown on Fig. 8.

recirculation dominates (Fig. 8c). Mode 1 explains 55.8% of the along-slope velocity anomaly. The mode-2 phase and amplitude spatial maps show an equatorward anomaly on the continental shelf and the EAC poleward along-slope anomaly detached from the continental shelf with the core of the EAC extending from 154° to 157°E (Figs. 8d,e). The EAC recirculation anomaly is only found at the far eastern edge of the mooring array. The velocity anomaly reconstruction clearly shows the strong anomalous equatorward velocity on the continental shelf, the EAC located on the outer edge of the continental slope and extending over the abyssal plain to 154.9°E, and the EAC recirculation at the far eastern edge of the mooring array (Fig. 8f). Mode 2 explains 16.3% of the along-slope velocity anomaly. The first two leading modes explain 72.1% of the velocity anomaly. Modes 3 and 4 explain 8.4% and 6.6% of the along-slope velocity anomaly, respectively (Fig. 8). While both modes show an anomalous equatorward flow on the continental shelf and the EAC located over or off the continental slope, the complexity of the deep-ocean variability is evident in mode 3 and to a lesser extent in mode 4 (Figs. 8i,l).

The normalized power spectrum of the principle components of the first four modes show that modes 1 and 2 are associated with longer period variability with spectral peaks at 60 and 120 days, respectively (Figs. 9a,b). Modes 3 and 4, while still having spectral peaks at longer periods, have peaks at periods less than 50 days. In particular, mode 3 has spectral peaks near 15 to 30 days (Figs. 9c,d). This indicates that for this short time series, the modes 1 and 2 are distinguished from modes 3 and 4 in their spectral qualities. The first two modes are dominated by longer-term variability and modes 3 and 4 capture the shorter-term variability and movement of the EAC.

The COEF analysis shows that the EAC has two preferred states: in the first mode the core of the EAC is located on the continental slope with the equatorward EAC recirculation essentially restricting the offshore extension of the poleward EAC flow, and the second mode has the poleward EAC flow located offshore of the continental slope and equatorward velocity inshore of the EAC core. In the second mode the equatorward EAC recirculation is at the eastern edge of the current meter array. Mode 1 is dominant at periods of approximately 60 days, and mode 2 is dominant at periods of 120 days. Clearly the length of the EAC time series available is relatively short, and while this application of CEOF analysis is beginning to distinguish EAC modes, a longer time series will improve the separation and important characteristics of the dominant modes. Indeed, Sloyan and O'Kane (2015), show that decadal variability in the EAC is associated with the baroclinic instability of the Pacific basin. Thus, determining and characterizing the modes of EAC variability will require a multidecadal time series.

4. The EAC mass and heat transports

From the interpolated 18-month time series of along-slope velocity and temperature, and the area occupied by the mooring array, we calculate the EAC mass and heat transport (Fig. 10). Here, we present the integral of the mass and heat transport for different vertical layers: poleward above 2000 m, net transport above 2000 m, and total full depth. The 18-month mean mass and heat transport and their standard deviations are provided in Tables 3 and 4. The difference in the poleward and net mass and heat transports above 2000 m reflects the presence of equatorward flow on the continental shelf and equatorward flow of the EAC retroflection at the eastern end of the mooring array.

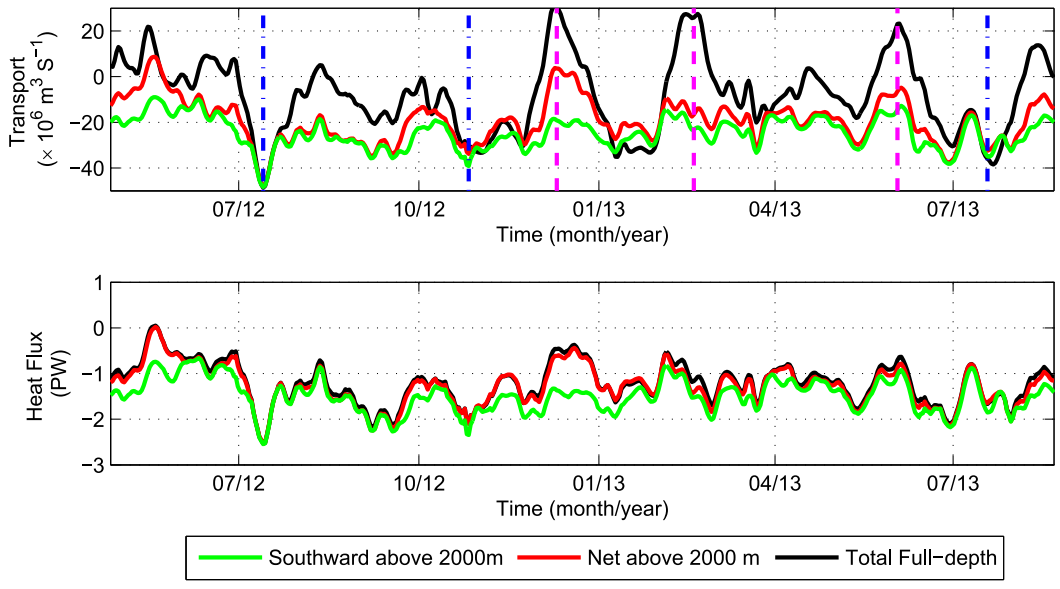

FIG. 10. The EAC 18-month mass (Sv) and heat transport (PW) time series. Dashed vertical lines indicate time when the time series transports were strongly poleward (blue) and weakly poleward or reversed (magenta). Associated along-slope velocity distribution is shown in Fig. 7.

The poleward-only mass transport above 2000 m varies between 45.4 and 3.3 Sv, with a mean mass transport of 22.1 ± 7.5 Sv (Table 3). The net mass transport above 2000 m varies between −44.7 and 8.0 Sv, with a mean mass transport of −15.8 ± 10.5 Sv. There are periods in the time series when the poleward EAC transport dominates, that is, the equatorward EAC recirculation is weak and only found at the far eastern edge of the mooring array (Fig. 10, blue dashed lines). In general, the equatorward transport of the EAC recirculation has a mean mass transport of 6.3 Sv. However, there are periods in the 18-month time series when the EAC recirculation is stronger than or of similar magnitude to that of the poleward EAC transport, resulting in a near zero or net equatorward transport across the mooring array above 2000 m (Fig. 10; Table 3).

For interest, we also show the total full-depth mass transport. When considering the difference between the net mass transport above 2000 m and the full-depth transport, we find that there are sporadic periods of strong equatorward mass transport below 2000 m that result in a full-depth equatorward mass transport across the mooring array (Fig. 10, magenta dashed lines). Mata et al. (2000), at 30°S, also find periods of strong deep equatorward transport that resulted in a full-depth equatorward flow. The drivers of and relationship to the upper 2000-m variability of these sporadic strong deep currents and transports will be a topic of future investigations.

As expected the heat transport of the EAC is dominated by the balance between the poleward EAC and equatorward EAC recirculation transport (Fig. 10). The mean poleward heat transport and flow-weighted temperature above 2000 m are 1.35 ± 0.42 PW and 15.33°C, respectively, and the net heat transport and flow-weighted temperature above 2000 m are −1.11 ± 0.51 PW and 17.56°C, respectively (Table 4). The mean equatorward heat transport associated with the EAC recirculation is 0.24 PW; however, the EAC recirculation can reduce the poleward heat transport across the array by as much as 1 PW during periods of strong EAC recirculation (Fig. 10).

To explore the relationship between the mass transport and the identified major modes, we compare the mass transport time series with the temporal amplitude to the COEF 1 to 4 modes (Fig. 11). Significant correlations (P-value, $P < 0.05$) are found among the poleward mass transport above 2000 m and mode 1 (correlation coefficient, $R = 0.26$), mode 2 ($R = 0.22$), and mode 3 ($R = 0.13$), net

TABLE 3. EAC mean, standard deviation, maximum, and minimum volume transport (Sv) from the mooring array time series. Negative values are poleward.

Depth range	Mean	STD	Minimum	Maximum
0–2000 m				
net transport	−15.8	±10.5	−44.7	8.0
poleward transport	−22.1	±7.5	−45.4	−3.3
2000 m–bottom				
transport	13.3	±10.2	−11.7	45.4
Full-depth				
transport	−2.5	±16.5	−41.6	34.6

TABLE 4. EAC mean and standard deviation heat transport (PW; 1 PW = 10^{15} W), flow-weighted temperature (°C) and eddy heat flux (PW) from the mooring array time series. Negative values are poleward.

Depth range	Mean Heat	STD	Flow-weighted temperature	Eddy heat
0–2000 m				
net transport	−1.11	±0.51	17.56	0.01
poleward transport	−1.35	±0.42	15.33	0.003
2000 m–bottom				
transport	0.08	±0.06	1.42	0.0001
Full-depth				
transport	−1.04	±0.52		0.01

transport above 2000 m and mode 1 ($R = 0.16$) and mode 2 ($R = 0.19$), and the total full-depth transport and mode 1 ($R = 0.19$) and mode 2 ($R = 0.13$). As the spatial pattern of modes 1 and 2 suggest, these modes are related to the temporal variability of mass transport above 2000 m and the position and strength of the poleward EAC transport and equatorward continental shelf and EAC recirculation transport.

5. Mean and eddy kinetic energy

The previous attempt to monitor the EAC, using a mooring array at 30°S, found that the mean and standard deviation of the transport were of comparable magnitude (Mata et al. 2000). Considering the results from the previous mooring array (Mata et al. 2000), from other observations (Ridgway and Dunn 2003) and analyses of ocean models (O'Kane et al. 2011), the mooring array was located at 27°S, where we anticipated that the mean velocity would dominate, enabling a mooring array to effectively monitor the EAC property transports (K. R. Ridgway and B. M. Sloyan 2011, unpublished manuscript). To assess the degree to which the mooring array achieves this goal, we calculate the mean kinetic energy (MKE) and eddy kinetic energy (EKE). The MKE is

$$\mathrm{MKE} = \frac{1}{2}(\overline{u}^2 + \overline{v}^2), \tag{1}$$

where $\overline{u}^2$ and $\overline{v}^2$ are the time-mean velocity components, and EKE is

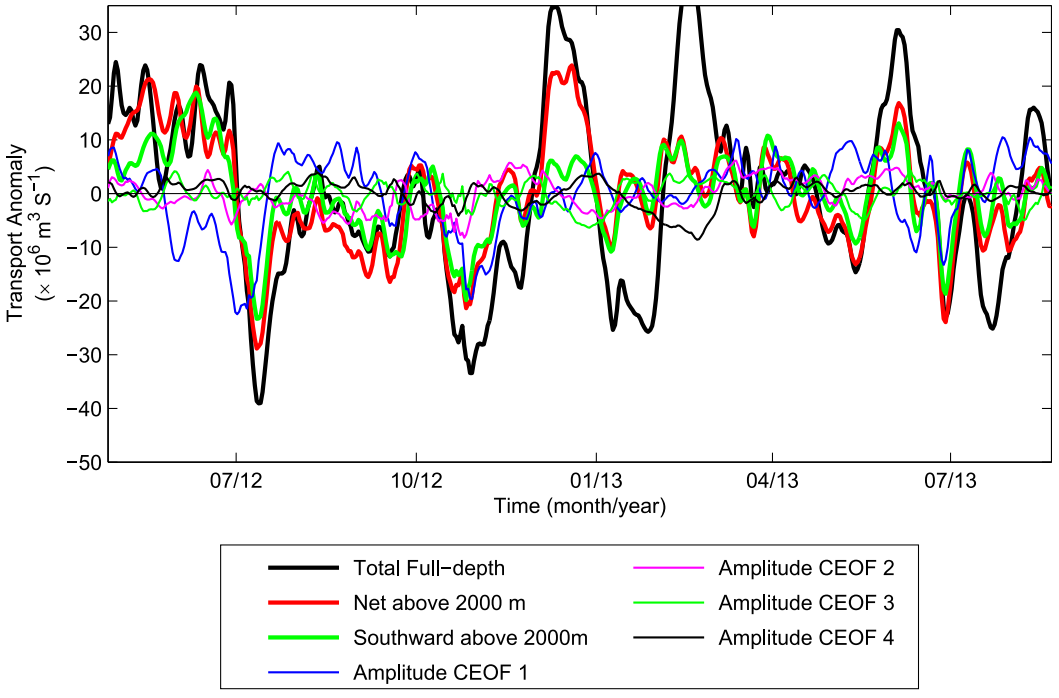

FIG. 11. Comparison of the EAC 18-month transport with the complex EOF mode-1, mode-2, mode-3, and mode-4 temporal amplitude.

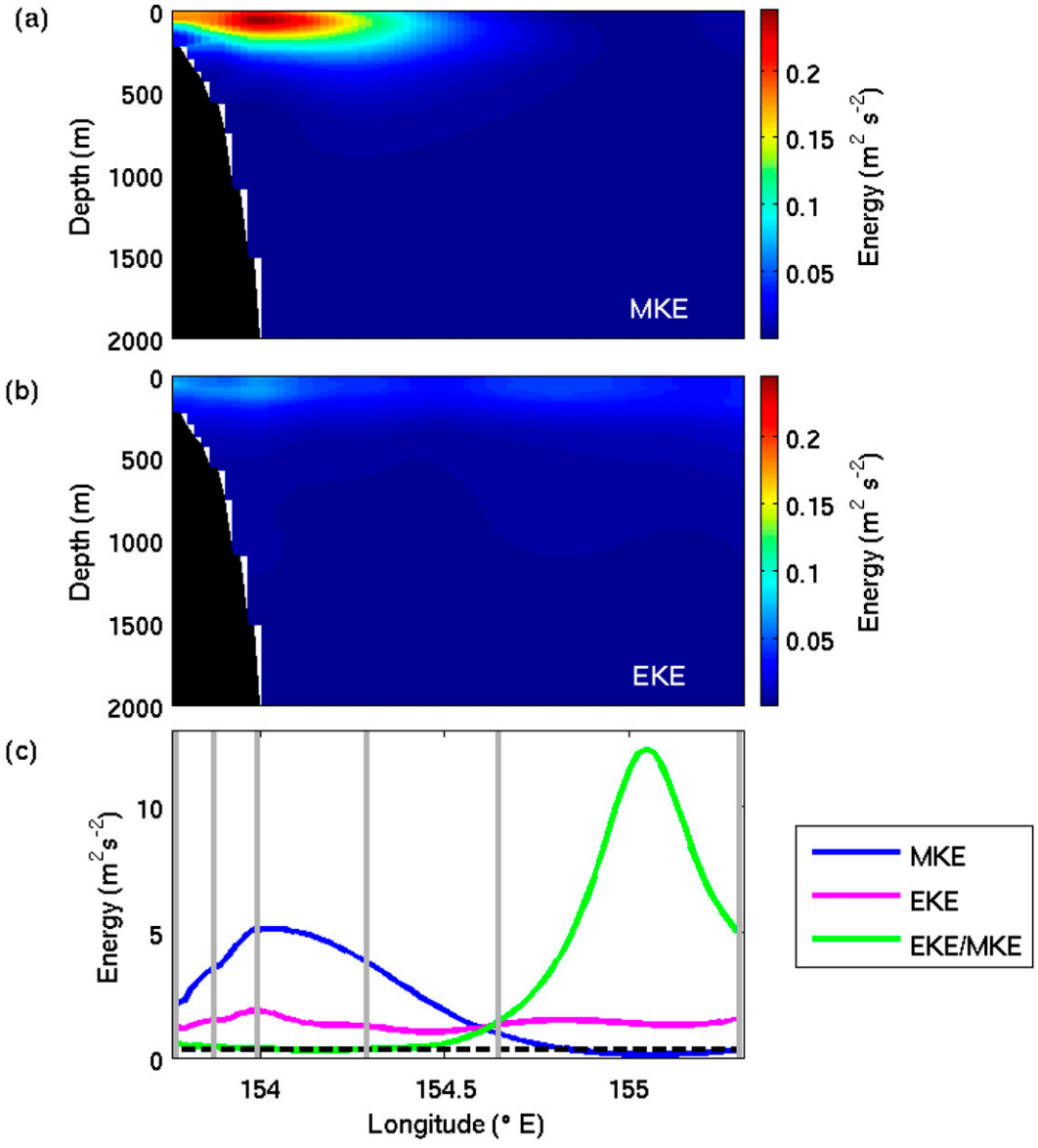

FIG. 12. EAC vertical and horizontal distribution of the (a) MKE ($m^2\,s^{-2}$), (b) EKE ($m^2\,s^{-2}$), and (c) the 0–2000-m depth integral of the MKE (blue), EKE (magenta), and the EKE:MKE ratio (green). Also shown is the ratio of EKE:MKE = 1/3 (black dashed line); an EKE:MKE ratio greater than 1/3 indicates a variable current system.

$$\mathrm{EKE} = \frac{1}{2}(u'^2 + v'^2), \tag{2}$$

where u'^2 and v'^2 are velocity anomalies.

The distribution of MKE and EKE from the continental shelf to 154.64°E shows that in the core of the EAC the MKE is an order of magnitude larger than EKE (Figs. 12a,b). East of 154.64°E, above 1000 m, the EKE becomes larger than the MKE. The transition from dominant MKE to dominant EKE is clearly shown by the EKE:MKE ratio (Fig. 12c). The EKE:MKE ratio has low values (1 or less) westward of 154.64°E, indicating that the mooring array is observing a stable EAC. Eastward of 154.64°E, the EKE:MKE ratio increases to greater than 10, showing that the outer edge of the array observes a more variable current system resultant from the west–east wavering of the poleward EAC and equatorward EAC recirculation across the mooring array. Although there is a relative increase in the EKE:MKE ratio at the eastern edge of the mooring array, the ratio is much smaller than the EKE:MKE ratio (10^2–10^3) found farther south along the Australian eastern boundary and in other EKE dominated regions (Scharffenberg and Stammer 2010). The EKE:MKE

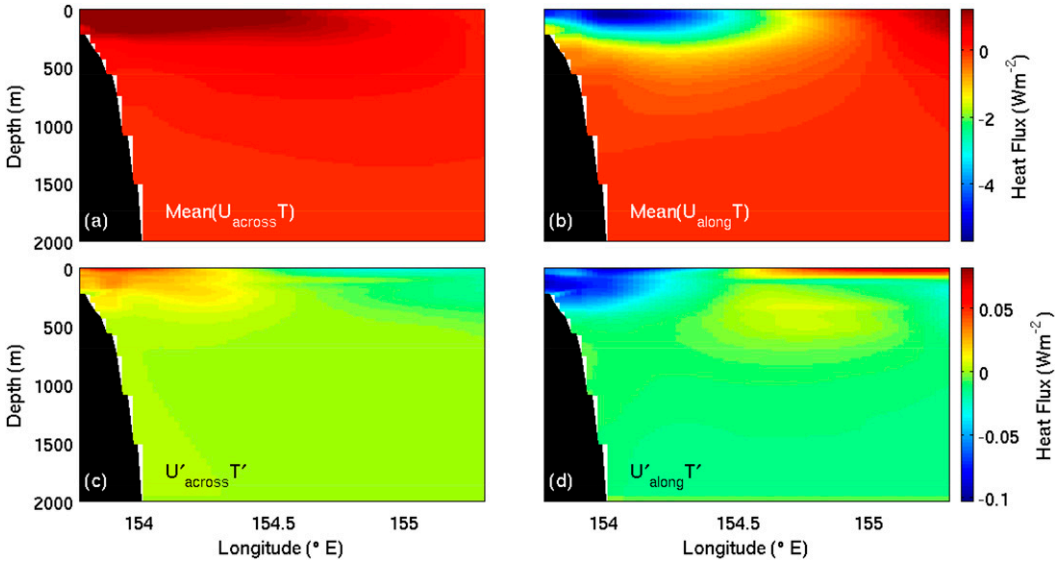

FIG. 13. EAC (a),(b) mean and (c),(d) eddy heat fluxes (W m^{-2}) in the (left) across- and (right) along-slope direction. Note the different color scales for the top and bottom rows.

ratio at the eastern edge of the mooring array is comparable to the global average of 6–7 (Scharffenberg and Stammer 2010).

6. Discussion

This study uses the IMOS EAC mooring array to provide the first estimates of the mean and variability of the EAC property transport at 27°S. The mooring array captures the complete longitudinal extent of the poleward EAC flow 97% of the time between April 2012 and August 2013. The exception is a 9-day period between 21 July and 1 July 2012 when the poleward EAC flow is at the eastern edge of the mooring array (EAC_M5). The EAC poleward core then propagates westward across the mooring array between 2 and 15 July 2012, such that by 16 July 2012 the poleward EAC core is located at the time series mean position. The analysis of the data from the IMOS EAC mooring array finds an 18-month mean poleward-only mass transport above 2000 m is 22.1 ± 7.5 Sv, and the net mass poleward transport above 2000 m is 15.8 ± 10.5 Sv. The strength of the EAC is comparable to other western boundary currents: the Agulhas Current is −69.7 ± 4.3 Sv (Bryden et al. 2005; Imawaki et al. 1983), the Gulf Stream (at Florida Strait) is 31 Sv (Baringer and Larsen 2001; Imawaki et al. 1983), the Kuroshio Current in large and nonlarge meander mode is 24 and 23.5 Sv, respectively (Kawabe 1995; Imawaki et al. 1983), and the Brazil Current is −11 Sv (Imawaki et al. 1983).

From the 18-month time series, we find that the EAC at 27°S is characterized by a strong poleward velocity with a subsurface maximum whose positions propagate across the mooring array and an offshore equatorward recirculation. Between 15° and 24°S, Ridgway and Dunn (2003) find a subsurface current maximum of 0.15 m s^{-1} at approximately 100-m depth. At 27°S, we find that the subsurface maximum velocity has increased in strength to greater than 0.6 m s^{-1}. Farther south there is no observational evidence of a subsurface velocity maximum (Mata et al. 2000; Ridgway and Dunn 2003); however, some model studies do identify a subsurface velocity maximum (Roughan et al. 2003).

The mean poleward-only heat transport and flow-weighted temperature above 2000 m are 1.35 ± 0.42 PW and 15.33°C, respectively, and the net heat transport and flow-weighted temperature above 2000 m are −1.11 ± 0.51 PW and 17.56°C, respectively. This heat transport is dominated by the mean along-slope heat transport (Fig. 13). The mean along-slope heat transport is 6 times larger than the mean across-slope heat transport and nearly two orders of magnitude larger than the along-slope and across-slope heat transport variability (Fig. 13). The dominant, mean, poleward, along-slope mass and heat transports and small MKE: EKE ratio indicate that the IMOS EAC mooring array provides a robust estimate of the EAC property transport at 27°S. This strongly supports the locations and design of the IMOS mooring array for the sustained monitoring of the EAC.

At 27°S, we find that the EAC system is dominated by two modes: EAC located on the continental shelf and slope and an offshore strong EAC recirculation and EAC located offshore of the continental slope with a

weak EAC recirculation and an equatorward flow on the continental shelf. Mode 1 is dominant at periods of approximately 60 days, and mode 2 is dominant at periods of 120 days. Many previous studies (observational and model based) find spectral energy peaks at periods of 90 to 180 days (Mata et al. 2000; Bowen et al. 2005; Mata et al. 2006; Wilkin and Zhang 2007). These previous studies have generally focused on the separation region of the EAC (31°–35°S) and poleward propagation of eddies. Bowen et al. (2005) suggest that the variability originates at the separation area and is amplified by local instabilities. Using CEOF analysis, Wilkin and Zhang (2007) identified two modes of EAC variability: an eddy mode that is associated with local flow instability and a wave mode that is related to onshore (westward) propagation but that, because of the model boundary configuration, was not adequately represented. Results from this study suggest that there may be a link between the EAC at 27°S and the behavior farther south in the separation zone. However, we remind the reader that the COEF analysis is undertaken on a relatively short time series.

7. Conclusions

The IMOS East Australian Current mooring array at 27°S has provided the first comprehensive full-depth monitoring of the East Australian Current velocity and derived mass and heat transport. While the initial deployment of the mooring array was for 18 months between April 2012 and August 2013, the mooring array was reestablished in May 2015 when a slightly modified six mooring array was deployed at a very similar location. It is planned that the mooring array will be turned around on an 18-month schedule for the foreseeable future.

The continued monitoring of the EAC is central to our understanding of how climate signals are communicated through the global ocean. Understanding the frequency and drivers of the major EAC modes and their impact on the downstream EAC evolution and interaction with the coastal shelf currents and EAC separation zone will be the subject of further study. It is hoped that joint observation and modeling studies will provide significant insight into the dynamical interactions between the EAC and the basin scale and local shelf ocean circulation.

Acknowledgments. We thank two anonymous reviewers for their constructive comments that improved the manuscript. The work was supported by the Australian Climate Change Science Program collaboration between the Australian Department of Environment and CSIRO Ocean and Atmosphere. The mooring array was funded by the Integrated Marine Observing System (www.imos.org.au) and CSIRO Oceans and Atmosphere Flagship. Mooring data used in this paper are available from the Integrated Marine Observing System (IMOS; https://imos.aodn.org.au/imos123/home) and OceanSITES (http://www.oceansites.org).

REFERENCES

Baringer, M. O., and J. Larsen, 2001: Sixteen years of Florida Current transport at 27°N. *Geophys. Res. Lett.*, **28**, 3179–3182, doi:10.1029/2001GL013246.

Boland, F. M., and B. V. Hamon, 1970: The East Australian Current, 1965–1968. *Deep-Sea Res. Oceanogr. Abstr.*, **17**, 777–794, doi:10.1016/0011-7471(70)90041-0.

——, and J. A. Church, 1981: The East Australian Current 1978. *Deep-Sea Res.*, **28A**, 937–957, doi:10.1016/0198-0149(81)90011-X.

Bowen, M. M., J. L. Wilkin, and W. J. Emery, 2005: Variability and forcing of the East Australian Current. *J. Geophys. Res.*, **110**, C03019, doi:10.1029/2004JC002533.

Bryden, H. L., L. M. Beal, and L. M. Duncan, 2005: Structure and transport of the Agulhas Current and its temporal variability. *J. Oceanogr.*, **61**, 479–492, doi:10.1007/s10872-005-0057-8.

Cetina-Heredia, P., M. Roughan, E. van Sebille, and M. Coleman, 2014: Long-term trends in the East Australian Current separation latitude and eddy driven transport. *J. Geophys. Res. Oceans*, **119**, 4351–4366, doi:10.1002/2014JC010071.

Cowley, R., 2015: Report on the quality control of IMOS ABOS East Australian Current (EAC) Deep Water moorings array. CSIRO Ocean and Atmosphere Flagship Tech., 124 pp. [Available online at http://data.aodn.org.au/IMOS/public/ABOS/reports/IMOS_ABOS_EAC_2012_13_QCreportV2.pdf.]

Everett, J. D., M. E. Baird, P. R. Oke, and I. M. Suthers, 2012: An avenue of eddies: Quantifying the biophysical properties of mesoscale eddies in the Tasman Sea. *Geophys. Res. Lett.*, **39**, L16608, doi:10.1029/2012GL053091.

——, ——, M. Roughan, I. M. Suthers, and M. A. Doblin, 2014: Relative impact of seasonal and oceanographic drivers on surface chlorophyll *a* along a western boundary current. *Prog. Oceanogr.*, **120**, 340–351, doi:10.1016/j.pocean.2013.10.016.

Ganachaud, A., and Coauthors, 2014: The Southwest Pacific Ocean Circulation and Climate Experiment (SPICE). *J. Geophys. Res. Oceans*, **119**, 7660–7686, doi:10.1002/2013JC009678.

Hannachi, A., I. T. Jolliffe, and D. B. Stephenson, 2007: Empirical orthogonal functions and related techniques in atmospheric science: A review. *Int. J. Climatol.*, **27**, 1119–1152, doi:10.1002/joc.1499.

Imawaki, S., A. S. Bower, L. Beal, and B. Qui, 1983: Western boundary currents. *Ocean Circulation and Climate: A 21st Century Perspective*, G. Siedler et al., Eds., Elsevier, 305–330.

Kawabe, M., 1995: Variations of current path, velocity and volume transport of the Kuroshio in relation with large meander. *J. Phys. Oceanogr.*, **25**, 3103–3117, doi:10.1175/1520-0485(1995)025<3103:VOCPVA>2.0.CO;2.

Mata, M., M. Tomczak, S. Wijffels, and J. A. Church, 2000: East Australian Current volume transports at 30°S: Estimates from the World Ocean Circulation Experiment hydrographic sections PR11/P6 and the PCM3 current meter array. *J. Geophys. Res.*, **105**, 28 509–28 526, doi:10.1029/1999JC000121.

——, S. Wijffels, J. Church, and M. Tomczak, 2006: Eddy shedding and energy conversions in the East Australian Current. *J. Geophys. Res.*, **111**, C09034, doi:10.1029/2006JC003592.

O'Kane, T. J., P. A. Oke, and P. A. Sandary, 2011: Predicting the East Australian Current. *Ocean Modell.*, **38**, 251–266, doi:10.1016/j.ocemod.2011.04.003.

Oliver, E. C. J., and N. J. Holbrook, 2014: Extending our understanding of South Pacific Gyre "spin-up": Modeling the East Australian Current in a future climate. *J. Geophys. Res.*, **119**, 2788–2805, doi:10.1002/2013JC009591.

Ridgway, K. R., 2007: Long-term trend and decadal variability of the southward penetration of the East Australian Current. *Geophys. Res. Lett.*, **34**, L13613, doi:10.1029/2007GL030393.

——, and J. R. Dunn, 2003: Mesoscale structure of the mean East Australian Current System and its relationship with topography. *Prog. Oceanogr.*, **56**, 189–222, doi:10.1016/S0079-6611(03)00004-1.

——, ——, and J. L. Wilkin, 2002: Ocean interpolation by four-dimensional weighted least squares—Application to the waters around Australasia. *J. Atmos. Oceanic Technol.*, **19**, 1357–1375, doi:10.1175/1520-0426(2002)019<1357:OIBFDW>2.0.CO;2.

——, R. C. Coleman, R. J. Bailey, and P. Sutton, 2008: Decadal variability of East Australian Current transport inferred from repeated high-density XBT transects, a CTD survey and satellite altimetry. *J. Geophys. Res.*, **113**, C08039, doi:10.1029/2007JC004664.

Roemmich, D., J. Gilson, J. Willis, P. Sutton, and K. Ridgway, 2005: Closing the time-varying mass and heat budgets for large ocean areas: The Tasman Box. *J. Climate*, **18**, 2330–2343, doi:10.1175/JCLI3409.1.

Roughan, M., P. R. Oke, and J. H. Middleton, 2003: A modeling study of the climatological current field and the trajectories of upwelled particles in the East Australian Current. *J. Phys. Oceanogr.*, **33**, 2551–2564, doi:10.1175/1520-0485(2003)033<2551:AMSOTC>2.0.CO;2.

Scharffenberg, M. G., and D. Stammer, 2010: Seasonal variations of the large-scale geostrophic flow field and eddy kinetic energy inferred from the TOPEX/Poseidon and Jason-1 tandem mission data. *J. Geophys. Res.*, **115**, C02008, doi:10.1029/2008JC005242.

Sloyan, B. M., and T. J. O'Kane, 2015: Drivers of decadal variability in the Tasman Sea. *J. Geophys. Res. Oceans*, **120**, 3193–3210, doi:10.1002/2014JC010550.

Tilburg, C., H. H. Hurlburt, J. O. Brien, and J. Shriver, 2001: The dynamics of the East Australian Current system: The Tasman Front, the East Auckland Current, and the East Cape Current. *J. Phys. Oceanogr.*, **31**, 2917–2943, doi:10.1175/1520-0485(2001)031<2917:TDOTEA>2.0.CO;2.

Wilkin, J. L., and W. G. Zhang, 2007: Modes of mesoscale sea surface height and temperature variability in the East Australian Current. *J. Geophys. Res.*, **112**, C01013, doi:10.1029/2006JC003590.